plication of Lasers", ed., C. B. Moore, (Academic Press, New York, 1979) Vol. 4, Chapter 5; (b) "Surface Enhanced Raman Scattering", R. K. Chang and T. E. Furtak, eds. (Plenum Press, New York, 1982); (c) R. L. Birke, J. R. Lombardi, and L. A. Sanchez, In "Electrochemical of Biological Redox Components", ed., K. M. Kadish, (American Chemical Society, Washington DC, 1982) Adv. Chem. Ser. No. 4; (d) M. Moskovits, *Rev. Mod. Phys.* **57**, 782-826 (1985).
2. (a) T. M. Cotton, S. G. Schultz, and R. P. Vand Duyne, *J. Am. Chem. Soc.*, **102**, 7960 (1980); (b) T. M. Cotton, R. Timkovich, and M. S. Cork, *FEBS Lett.* **147**, 81 (1982); (c) J. S. Suh, D. P. DiLella, and M. Moskovits, *J. Phys. Chem.* **87**, 1540 (1983).
3. (a) G. M. Goncher and C. B. Harris, *J. Phys. Chem.* **77**, 3767 (1982); (b) C. J. Chen and R. M. Osgood, *Phys. Rev. Lett.* **50**, 1705 (1983); (c) G. M. Goncher, C. A. Parsons, and C. B. Harris, *J. Phys. Chem.* **88**, 4200 (1984); (d) J. S. Suh and K. H. Michaelian, *J. Phys. Chem.* **91**, 598 (1987); (e) T. H. Joo, Y. H. Yim, K. Kim, and M. S. Kim, *J. Phys. Chem.* **93**, 1422 (1989).
4. G. Smulevich and T. G. Spiro, *J. Phys. Chem.* **89**, 5168 (1985).
5. J. de Groot and R. E. Hester, *J. Phys. Chem.* **91**, 1693 (1987).
6. (a) M. Kim, T. Tsujino, and K. Itoh, *Chem. Phys. Lett.*, **125**, 364 (1986); (b) K. Itoh, T. Sugii, and M. Kim, *J. Phys. Chem.* **92**, 1568 (1988).
7. O. K. Song, M. Yoon, J. R. Chang, and D. Kim, *Bull. Kor. Chem. Soc.* **10**, 39 (1989).
8. O. K. Song, M. Yoon, and D. Kim, *J. Raman Spectrosc.*, **20**, 739 (1989).
9. (a) G. N. LaMar, G. R. Eaton, R. H. Holm and F. A. and Walker, *J. Am. Chem. Soc.* **95**, 63 (1973); (b) S. S. Eaton and G. R. Eaton, *J. Am. Chem. Soc.* **97**, 3660 (1975).
10. Fore reviews (a) T. G. Spiro In "Iron Porphyrins", A. B. P. Lever and H. B. Gray eds., Addison-Wesley, Reading, MA (1983), Part II, pp. 89-159; (b) S. A. Asher, *Method Enzymol.* **76**, 371 (1981); (c) R. H. Felton and N.-T. Yu, In "The Porphyrins", D. Dolphin ed., *Academic Press, New York* **III**, 347-393 (1978); (d) T. Kitagawa and Y. Ozaki *Struct. Bonding* **64**, 71 (1987).
11. N. Blom, J. Odo, K. Nakamoto, and D. P. Strommen, *J. Phys. Chem.* **90**, 2847 (1986).
12. (a) P. Stein, A. Ulman, and T. G. Spiro, *J. Phys. Chem.* **88**, 369 (1984); (b) J. M. Burke, J. R. Kincaid, and T. G. Spiro, *J. Am. Chem. Soc.* **100**, 6077 (1978); (c) N. Parthasarathi, C. Hansen, S. Yamaguchi, and T. G. Spiro, *ibid* **109**, 3865 (1987); (d) X.-Y. Li, R. S. Czernuszewicz, J.R. Kincaid, Y.O. Su and T. G. Spiro, *J. Phys. Chem.*, **94**, 31 (1990).
13. D. Kim, J. Terner, and T. G. Spiro, *J. Am. Chem. Soc.* **108**, 2097 (1986).
14. (a) S. Choi and T. G. Spiro, *J. Am. Chem. Soc.* **105**, 3683 (1983); (b) M. L. Mitchell, X.-Y. Li, J. R. Kincaid, and T. G. Spiro, *J. Phys. Chem.* **91**, 4690 (1987).
15. D. L. Willems and D. F. Bocian, *J. Am. Chem. Soc.* **106**, 880 (1984).
16. M. Abe, In "Spectroscopy of Biological Systems", eds. R. J. H. Clark and R. H. Hester, (John Wiley $ Sons, London, 1986) p. 347.
17. H. Nichols and R. M. Hexter, *J. Chem. Phys.* **75**, 3126 (1981).
18. M. Moskovits, *ibid* **77**, 4408 (1982).
19. V. M. Hallmark and A. Campion, *ibid* 84, 2942 (1986).
20. J. A. Creighton, *Surf. Sci.* **124**, 209 (1983).
21. P. Hildebrandt and T. G. Spiro, *J. Phys. Chem.* **92**, 3355 (1988).
22. L. A. Sanchez and T. G. Spiro, *J. Phys. Chem.* **89**, 763 (1985).
23. R. H. Felton, *in Ref.* **10**(c), Vol. V, pp. 53-125.
24. R. S. Czernuszewicz, Y. O. Su, M. K. Stern, K. A. Macor, D. Kim, J. T. Groves, and T. G. Spiro, *J. Am. Chem. Soc.* **110**, 4158 (1988).

Low Energy Ion-Surface Reactor

Won Yong Choi, Tae Hee Kang, and Heon Kang*

Department of Chemistry, Pohang Institute of Science and Technology, Pohang 790-600

Received January 22, 1990

Ion-surface collision studies at low kinetic energies (1-100 eV) provide a unique opportunity for investigating reactions and collision dynamics at surfaces. A special ion optics system for generating an energy- and mass-selected ion beam of this energy is designed and constructed. An ultrahigh vacuum (UHV) reaction chamber, in which the ions generated from the beamline collide with a solid surface, is equipped with Auger electron spectroscopy (AES) and thermal desorption spectrometry (TDS) as *in-situ* surface analytical tools. The resulting beam from the system has the following characteristics: ion current of 5-50 nA, energy spread <2 eV, current stability within $\pm 5\%$, and unit mass resolution below 20 amu. The performance of the instrument is illustrated with data representing the implantation behavior of Ar^+ into a graphite (0001) surface.

Introduction

The dynamics of atomic and molecular collisions on solid surfaces is a newly developing area where new experimental data, interpretations, and model calculations are constantly emerging. Especially, the interaction with surfaces in the low

energy (<100 eV) region is of special interest to chemists since it falls into energy range of chemical reactions. Supersonic molecular beams of thermal energy (below 1 eV) have been successfully used to gain insight into the microscopic mechanisms of inelastic scattering, trapping, and chemical reactions on surfaces.[1] In the hyperthermal energy region, however, few experimental works have been carried out because the highest energy attainable by a seeded molecular beam technique is limited below a few eV.[2] Ion beams are required in order to gain access to this region as the ions can be accelerated to any desired energy. However, there exists an experimental difficulty in transporting and focusing low energy (<100 eV) ion beams due to the beam divergence resulting from the space charge effect. Most of the ion beam studies to the present have been carried out at higher energies for such reasons, major efforts being put in ion scattering spectrometry (ISS) in keV regime[3] and ion implantation[4,5] (MeV region). Now that the reactive ions of <100 eV have become available, the area of low energy ion-surface interactions is fast growing as a unique method to study gas-surface reactions and its recent progress has been reviewed[6].

In our laboratory an instrument which meets the requirement for the study of low energy ion-surface interactons has been developed. This paper describes its construction and performance in detail. Because of the selectivity and specificity of the mass- and energy-selected ion beam for inducing surface reactions, this type of the instrument promises to be versatile for investigating many areas in ion beam researches: thin film deposition[7], chemical reactions at surfaces[8-10], low energy ion scattering[11,12] direct recoil spectrometry (DRS)[13], low energy sputtering[14,15], chemical sputtering or dry etching[16,17], passivation of metal surfaces[18,19], detection of intermediate states during surface reactions[20], and distinction of isomeric ions by surface-induced dissociation (SID)[21].

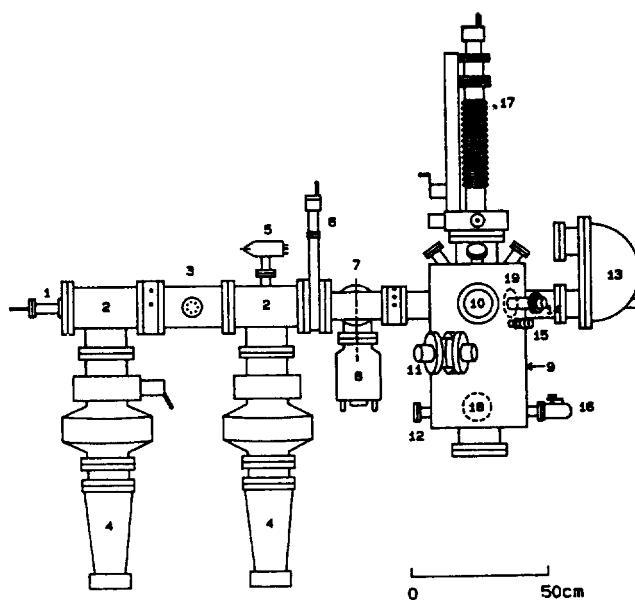

Figure 1. Side view of ion beamline and UHV chamber. The components labeled are: (1) ion source, (2) beamline vacuum housing, (3) Wien velocity filter, (4) oil diffusion pump with LN_2 trap, (5) ionization gauge, (6) gate valve, (7) 12° deflector, (8) turbomolecular pump, (9) UHV chamber, (10) viewport, (11) Residual Gas Analyzer (RGA), (12) nude ionization gauge, (13) 180° hemispherical energy analyzer, (14) Auger electron gun, (15) electron beam shielder, (16) leak valve, (17) long travel sample manipulator, (18) turbomolecular pumping port (backside), (19) sputter ion gun port (backside).

Instrument

General Description. The present system for the study of reactive ion beam-surface interactions mainly consists of a beamline which generates a mass- and energy-selected reactive ion beam and a UHV chamber in which ion-surface collision and *in-situ* surface characterization are carried out. The overall appearance of this system is presented in Figure 1.

The operational scheme is as follows. Gases are admitted into the source to generate ions, which are then extracted from the source and accelerated to a beam transfer kinetic energy. The ionic mixture in the beam is mass-selected by a velocity filter. The mass filtering of the ions is followed by 12° deflection to remove fast neutrals emanating from the neutralized ions. Just before the collision to the target surface, the ions are decelerated to a desired kinetic energy. Finally, an ion flux with a narrow kinetic energy distribution is directed onto the target surface. The reacted surface is investigated by Auger electron spectroscopy (AES) and thermal desorption spectrometry (TDS).

Reactive Ion Beamline. The schematic representation of the beamline and its associated electric circuitry is shown in Figure 2. In the followings the components of the beamline will be described in detail along the ion travel path, *i.e.*, from the ion source to the target. Gases to be ionized are leaked into the ionization chamber of the source through a variable leak valve (Granville Phillips), maintaining a discharge pressure of a few Torr. Colutron ion source, which is an electron impact discharge type, is used for ion production. Ions in the resulting plasma are extracted through a small aperture at the anode of the source (~0.5 mm diameter). Ions are subsequently focused and accelerated to a beam transfer kinetic energy (2 keV), in order to minimize the space charge dilation, by two focusing and accelerating lenses of a tube shape. Focusing at this stage aims at a 2 mm diameter aperture located just prior to the gate valve by adjusting the voltages of the lenses and steering plates. The lens geometry is designed according to an ion optics handbook[22].

The beam at this stage contains various chemical components and dissociation products. A single ionic species is required to be chosen for a selective ion-surface reaction. For this purpose, a Wien velocity filter (Coultron velocity filter model 600) is inserted in the beam path. It consists of an electro-magnet, a pair of electrical deflection plates and guard rings. The deflection plates are mounted between the two magnetic poles so that the directions of an electric field and a magnetic field are perpendicular. In this way only the ions experiencing a balanced force from the electric and magnetic fields can pass through the filter, resulting in m/e selection. The ion focusig effect, which limits the performance of the Wien-type filter, has been eliminated in the current design by introducing guard ring potentials. The Wien filter has some advantages over sector magnets em-

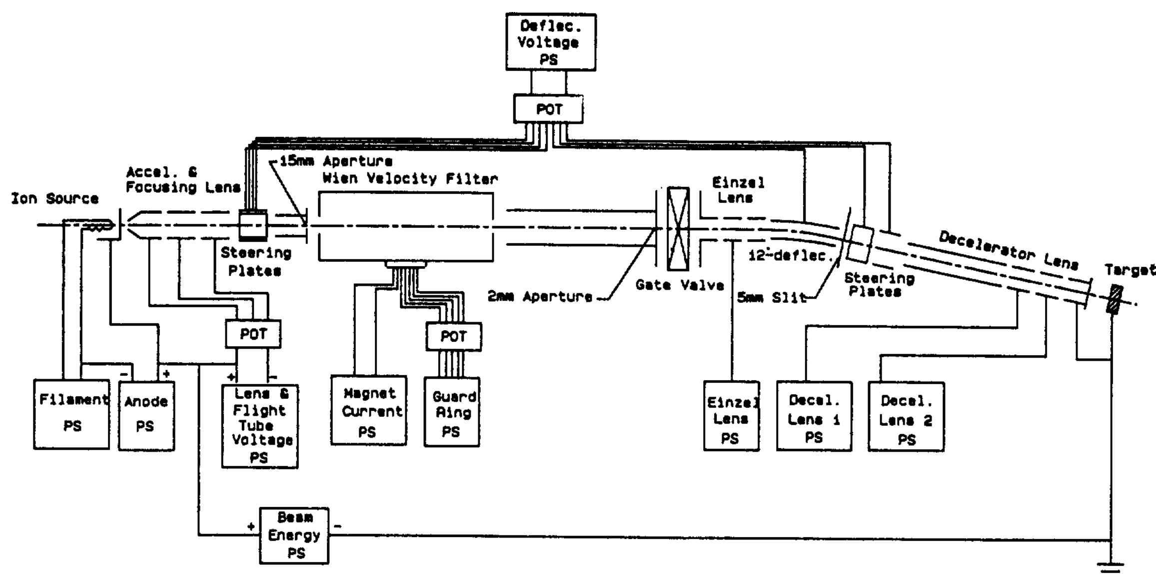

Figure 2. Schematic diagram and the associated circuitry of ion beamline. All the components of the beamline are floated at -2 kV with respect to the anode potential of the source except the extracting, focusing, and decelerating lenses although it is not shown for a simplified drawing.

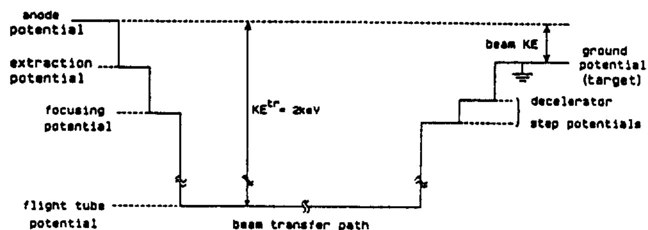

Figure 3. Potential profile along the beam trajectory.

ployed in previous designs[8,12,23] such as its lower price, compact size, and shorter beam travel path.

The ions that pass through the 2 mm aperture are refocused to the target by an einzel lens. The einzel lens is followed by a 12° deflector which is designed for the removal of the fast neutrals that may have survived up to this point or been generated *via* collision of ions with the wall. A slit of 5 mm × 10 mm is located after the deflector, followed by two pairs of steering plates for correcting the beam direction.

Up to this point, the ions are transferred with a beam transfer kinetic energy. Thus, it is necessary to decelerate the ions to a desired collision energy. This is done just before striking the surface, *i.e.*, in as short a distance as possible, in order to obtain a high ion current. The final collision energy is defined as the difference between the anode potential (ion source) and the ground potential (target). Figure 3 illustrates the above mentioned potential profile along the beam trajectory. Ions are transferred with a kinetic energy of 2 keV after being extracted from the source. Therefore, all the components of the beamline are floated at −2 kV with respect to the anode potential except the extracting, focusing, and decelerating lenses.

The gate valve with O-ring seal serves to block the ion beam, when the beam is not in use, without turning off the source, as well as to isolate the vacuum chamber from the beam line. However, the ground potential applied to the valve disturbs the original beam trajectory. So the ground

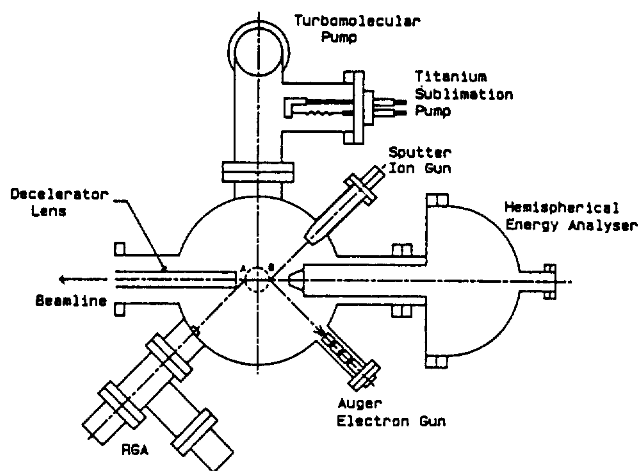

Figure 4. Top view of the UHV chamber and the attached components. A and B represent the sample positions for the beam exposure and AES analysis, respectively.

potential region is minimized by attaching a pair of large disks at the terminals of the cylindrical tube and the einzel lens as can be seen in Figure 2. The disks protrude into the gate valve as close as possible from both sides, thus preventing the disturbance of the field free path effectively.

The design of final deceleration lens is the most difficult part of the ion optics system. A single gap geometry[23] of a step potential decelerator was first tried, but unsuccessful in obtaining reasonable ion currents. In order to improve the ion current, two additional cylindrical lenses are inserted between the flight tube and the grounded cap, the final element. Their optimum bias voltages can be found by tuning to maximize the ion current. A 6 mm aperture at the grounded cap defines the spatial width of the beam. This deceleration lens protrudes into the chamber, ending at about 1 cm in front of the target as shown in Figure 4.

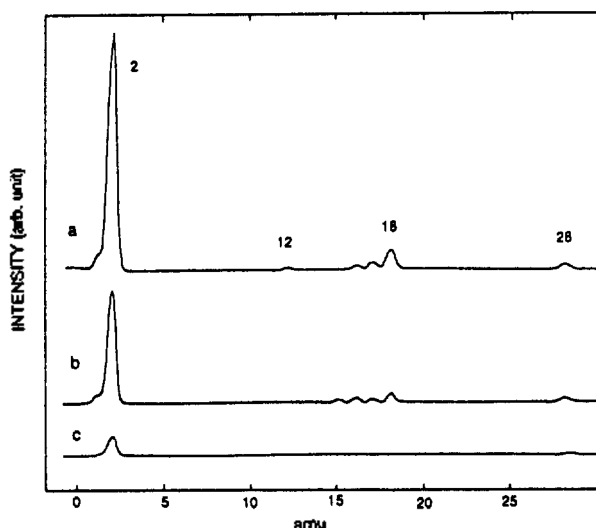

Figure 5. Residual gas components inside the UHV chamber. The mass spectra are taken: (a) after baking out (2×10^{-9} Torr), (b) immediately after TSP operation for 2 min, and (c) after overnight TSP operation (3×10^{-10} Torr).

Differential Pumping. The entire system is differentially pumped at four stages in order to reduce the pressure from a few Torr inside the source to a UHV ($\sim 10^{-10}$ Torr) in the analysis chamber.

The source region is pumped by a 600 *l*/sec oil diffusion pump with a liquid nitrogen trap. A separate diffusion pump of the same size is attached to the beam transport housing. The pressure in this region is measured by a Bayard-Alpert ionization gauge, the typical pressure in this region being $\sim 2 \times 10^{-6}$ Torr. The velocity filter is located between these two diffusion pumps (Figure 1), and its entrance is blocked except for a 15 mm diameter aperture which serves as a differential pumping baffle. A 345 *l*/sec turbomolecular pump (TMP) evacuates the deflector region. The 2 mm diameter aperture between the deflector region and the beamline, with the other parts being tightly sealed with an O-ring, reduces the pressure by two orders of magnitude from the beamline to the deflector region.

The collision/analysis chamber is pumped by a separate TMP (345 *l*/sec) and a home-made titanium sublimation pump (TSP). The 5×10 mm slit installed between the UHV chamber and the deflector region serves for pressure reduction. The TMP is mounted on a 6" port at the lower stage. An elbow connection is used in order to protect the pump from accidental dropping of tiny fractures off the sample manipulator and other parts. The TSP is attached in the middle of the elbow as depicted in Figue 4, and the titanium filament is off the pumping line in order to prevent the direct deposition of titanium vapor onto the sample surface. The residual gas components and the performance of the TSP is shown in RGA spectra of Figure 5. It can be noticed that the partial pressure of each component decreases with the operation of the titanium sublimator. The main constituent in this UHV environment is hydrogen largely due to the limit of the H_2 pumping speed of the TMP. The ultimate pressure attained by the combination of the TMP and the TSP is 3×10^{-10} Torr.

UHV Analysis Chamber. The UHV analysis chamber serves as a stage for sample manipulation and *in-situ* surface analysis (Figure 1). The entire body is made of 316 stainless steel with its internal surface electropolished. Copper gaskets are used for flange sealing. The chamber has a three stage (upper, middle, lower) structure along with the top and the bottom parts. The top view of the chamber with major attachments is presented in Figure 4.

A long-travel precision sample manipulator (Vacuum Science Workshop, VSW) is located at a 8" port on the top of the chamber. The sample is mounted at the end of the manipulator. The manipulator consists of an XYZ translator, a probe shaft, and a sample stage. It has a capability of long Z-directional translation (30 cm). By Z-axis translation the sample position is accessible to the middle stage as well as to the upper stage. The axial rotation of 360° enables the sample to be positioned at the two focal points (A and B in Figure 4). Daily operation starts at point A for ion beam exposure, then followed by 180° rotation to point B for AES analysis.

Sample heating is done by electron bombardment from a negatively biased (-2 keV) tungsten filament located behind the sample. Sample annealing temperature higher than 700°C can be achieved in this way. The temperature is measured by a chromel-alumel thermocouple.

Located above the target is a Faraday cup which is an essential equipment for the daily operation of the ion beam. The Faraday cup is used for locating the ion beam position, measuring the ion and electron current density, and probing the spatial beam distribution. It has a small entrance aperture (0.52 mm diam.) through which ions pass into the inner cup which is shaped to collect all the secondary electrons. The front face of the Faraday cup is covered with a copper foil which is conveniently used as a standard material for AES spectra.

A quadrupole mass spectrometer is attached to the chamber in order to perform TDS and residual gas analysis (RGA). The quadrupole mass spectrometer has a "T"-shaped geometry that a secondary electron multiplier (SEM) is located at 90° to the quadrupole filter axis. A nude ionization gauge for monitoring the pressure in the chamber is attached to the lower stage along with a variable leak valve and a 6" pumping port for the TMP. The leak valve (Varian) provides precisely controlled gas admission with leak rates as small as 1×10^{-10} Torr-*l*/sec. All of the parts are bakable to about 200°C using insulated nichrome wires wound around the whole chamber.

The chamber is equipped with an Auger electron spectrometer (AES) as an *in-situ* surface analytical tool (VSW). The primary electron beam for inducing Auger process is incident onto the sample surface at 45° relative to the surface normal. The ejecting secondary electrons in the direction of the surface normal are collected and energy analyzed by a hemispherical dispersive analyzer (see Figure 4). The primary electron beam, when not in use, is shielded from the target by an electron blocking plate attached to a rotary motion feedthrough so that unnecessary charging and damaging can be avoided.

The experimental setup of the AES with its circuity is schematically shown in Figure 6. The electrons that become monoenergetic by the dispersive analyzer strike the front surface of a channel electron multiplier. The amplified pulse signals are then transmitted *via* a pre-amplifier to a rate-

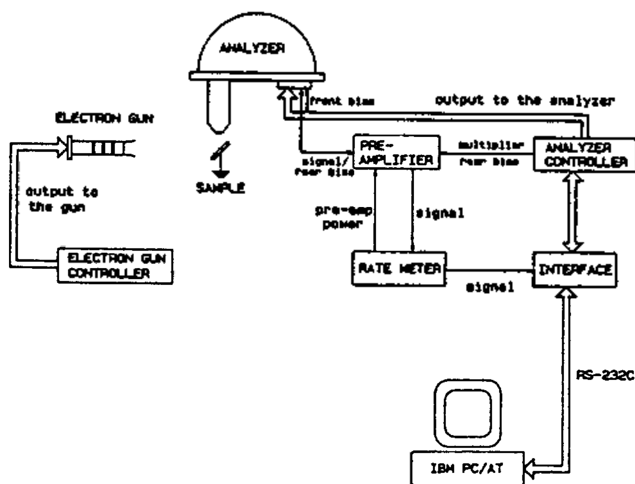

Figure 6. Experimental arrangement for Auger electron spectroscopy (AES).

Table 1. Characteristics of Ion Beam

ion source	Colutron ion source (electron impact plasma type)
kinetic energy	3~300 eV
transport kinetic energy	fixed at 2 keV
typical ion current	40 nA for Ar^+ at 100 eV
energy spread	<2 eV FWHM for Ar^+ and N_2^+
mass resolution of the velocity filter	$M/\Delta M \approx 22$
current stability	±5%
beam spot size	typically 1~2 mm diameter (variable)

meter where the counting rate (typically 100-200 kcounts/sec) is converted into an analog signal. Subsequently, the analog signal is digitized by an A/DC in the interface unit which transmits the digital data to an IBM AT personal computer through RS-232C communication. In this way, an integral spectrum (N(E) versus E) is recorded, which is subsequently differentiated numerically by a computer software program.

Performance of Ion Beam

Beam Characteristics. The characteristics of the ion beam are summarized in Table 1. The ion kinetic energy is variable from 3 to 300 eV. In Figure 7 the plot of Ar^+ ion current versus the beam energy is presented. Below 40 eV the current starts to decrease slowly with decreasing energy, while above this value it remains relatively constant. The Ar^+ ion current at 3 eV is about ~6 nA. Below this energy, it is usually difficult to obtain a significant amount of current density. A current of ~20 nA at 100 eV is routinely available and a current of up to ~50 nA can be obtained in a good condition. From other gases (N_2, He, Kr) similar current intensities are obtained. The ionization of N_2 gives rise to two ionic species, N_2^+ and N^+. The dissociated species N^+ gives an intensity about one order of magnitude lower than that of N_2^+, in accord with the reported electron impact ionization cross sections for N^+ and N_2^+.[24]

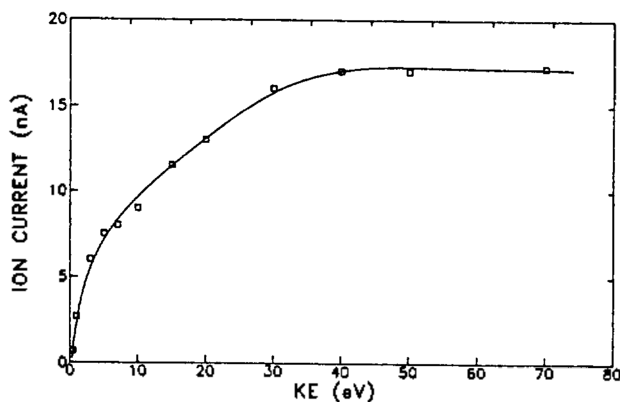

Figure 7. Plot of ion current (at target) of Ar^+ versus kinetic energy.

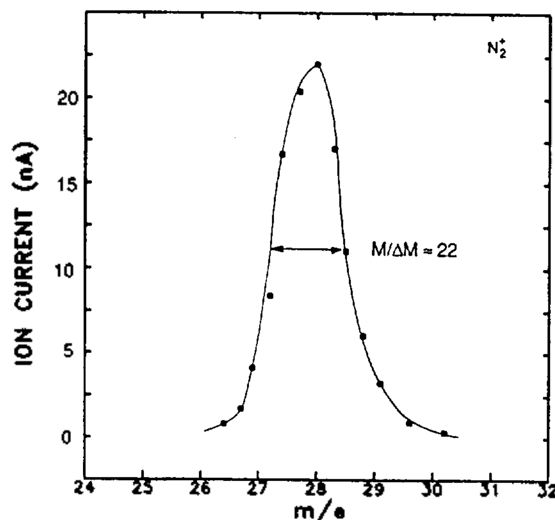

Figure 8. Mass spectrum of N_2^+ resolved by the Wien velocity filter. The mass selection is done by varying the magnet current while the deflection plate voltages are fixed.

The mass separation of the beam can be achieved through the velocity filter with a resolution of $M/\Delta M \approx 22$. This implies that the separation is possible between C^+, CH^+, CH_2^+, CH_3^+, and CH_4^+ from CH_4 discharge, not to mention N_2^+ and N^+ from N_2 gas. Figure 8 illustrates the resolving power of the filter for the N_2^+ beam.

A kinetic energy distribution of a beam is measured by directing the beam into the energy analyzer operated in a positive ion detection mode. It can be readily done in the present setup because the beam and the entrance slit of the analyzer are located on the same axis (Figure 4). Typical energy spectra of N_2^+ and N^+ are shown in Figure 9. The energy spread (FWHM) of N_2^+ is ~1.5 eV with a relatively symmetric profile. N^+ exhibits a similar energy spread but the profile contains a significant portion of a high energy tail. Such an asymmetric energy distribution of N^+ is qualitatively similar to the earlier result[25]. We may consider the following mechanisms for N^+ formation. Process (1) is the dissociation from an electronically excited N_2^+ *via* repulsive potential curves exhibiting an appearance potential of 24.3 eV[26]. Process (2) is the two electron ionization of N_2 followed by Coulombic separation.[25,27]

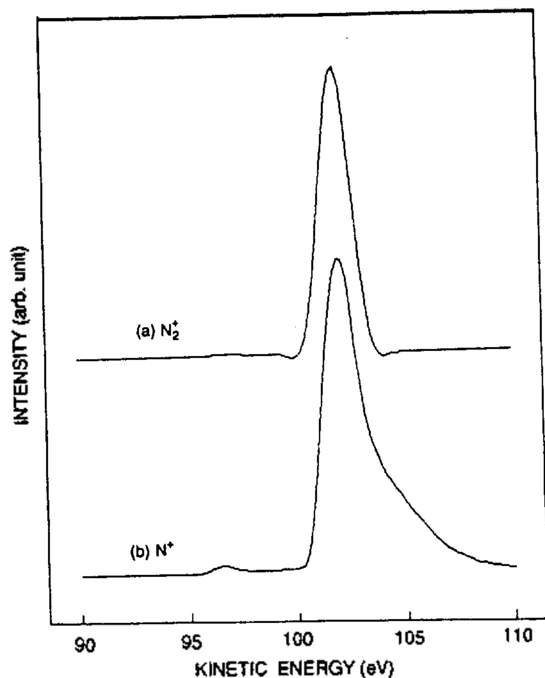

Figure 9. Kinetic energy distributions of (a) N_2^+ and (b) N^+ at the beam energy of 100 eV. The peak energies of the spectra do not match the beam energy because of the uncalibrated analyzer work function. The smaller peak at ~97 eV in (b) is an artifact possibly arising from surface-scattered ions inside the analyzer entrance channel.

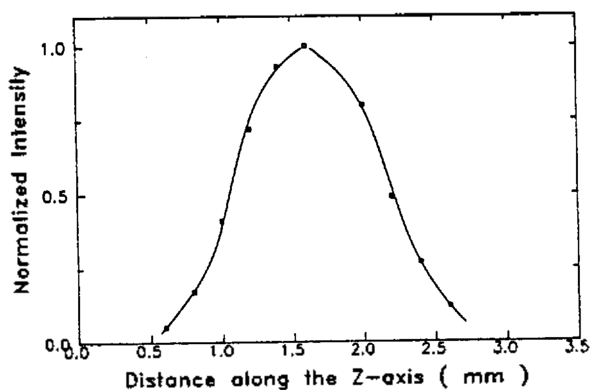

Figure 10. Spatial distribution of Ar^+ ion beam along the Z-direction. The ion intensities are normalized at the maximum value.

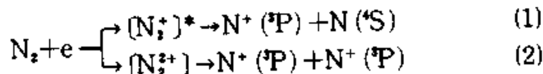

$$N_2 + e \rightarrow [N_2^+]^* \rightarrow N^+ (^3P) + N (^4S) \quad (1)$$
$$N_2 + e \rightarrow [N_2^{2+}] \rightarrow N^+ (^3P) + N^+ (^3P) \quad (2)$$

Franklin and Haney[28] have observed a process corresponding to (2), where the N^+ ions exhibit an appearance potential of 47.0 eV and a kinetic energy of 4.0 eV. This is in agreement with the potential curve for N_2^{2+} ($A^3\Pi_g$) calculated by Hurley[29]. Since the electron impact energy of 90 eV in the present experiment is well above the appearance potentials of both processes, we consider that the higher energy fragments are the consequence of the process (2). For Ar^+ and He^+ the energy spreads are ~1.9 eV and ~4 eV, respectively. The larger broadening for He^+ seems to result from more severe source discharge conditions (higher gas pressure, filament current, and electron impact energy) required

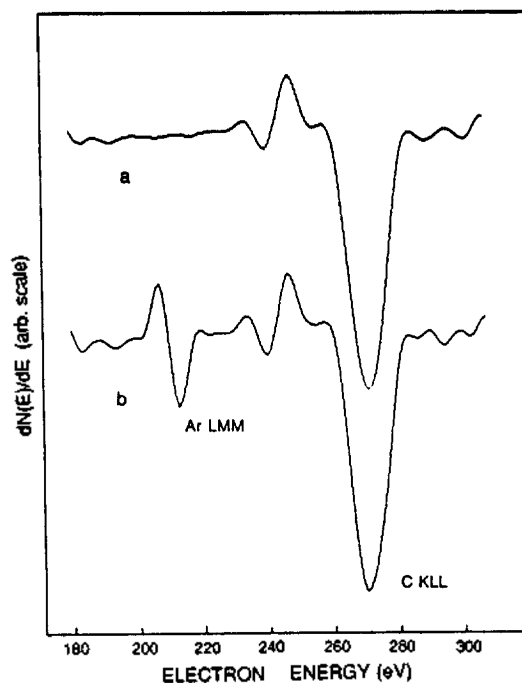

Figure 11. Auger spectra of (a) clean graphite before ion exposure and (b) Ar implanted graphite at 300 eV impact energy at a dose of 6.0×10^{15} ions/cm^2.

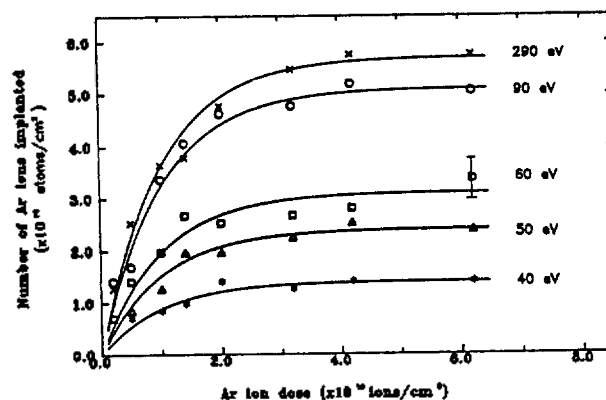

Figure 12. Implanted Ar concentration at different impact energies as a function of ion dose.

to maintain the helium discharge.

The beam currents are stable within ±5% over half an hour. Since most beam exposures in our experiments are shorter than 10 minutes, this stability is sufficient. The final spot size of the beam can be varied to give either focused or defocused beams by tuning the einzel lens. The spatial distribution of the beam is measured by translating the Faraday cup, one example being shown in Figure 10. A spot size of our favorite choice is ~2 mm.

Application to Ar^+ Implantation into Graphite. As an example of the performance of this instrument we describe here our study of low energy (<300 eV) Ar^+ ion implantation into a graphite (0001) surface. This system was chosen based upon the following considerations: (1) the interaction involving Ar^+ (neutralized near the surface[30]) is purely physical van der Waals type, and therefore the simplified binary collision approximation may be appropriate, (2) graphite has a high potence to accomodate guest atoms between its

layers, (3) at low energies the number of lattice atoms displaced during the collision is much less than at normal implantation energies (MeV). For such reasons, the graphite-noble gas ion system is a good candidate for studying physical implantation in a well defined situation. Furthermore, it is expected to form a prototype for future investigations on more complex reactive ion-surface interactions.

The implanted Ar concentration is measured as a function of ion dose. The clean surface is exposed to an Ar^+ beam at increasing doses, the implanted amount being monitored by AES between each dose. Figure 11 shows the Auger spectra for the clean and Ar^+ implanted graphite surfaces. The AES lineshapes are consistent with other reports from a single crystalline graphite.[31] The line shape remains unchanged upon the ion bombardment, indicating that structural damage is not severe.

The dose dependence of Ar concentration at five different impact energies are shown in Figure 12. The curves have a general shape which is convex upward, reaching a plateau at a saturation dose. At all energies the onset of saturation occurs at a dose of $\sim 2.0 \times 10^{15}$ ions/cm^2. At lower doses the ion impact leads either to trapping (implantation) or scattering into vacuum. The slope of the curve at a zero dose yields an initial trapping probability, the ratio of the number of trapped species to the number of incoming ions. As the lattice sites become occupied with Ar, a self-sputtering process, the ejection of the trapped Ar by Ar^+ impact, starts to compete with the trapping process. At a saturation dose the rates of trapping and self-sputtering become balanced, yielding an apparent trapping probability of zero. Such a behavior can be described by an exponentially rising curve (eq. 1) derived from a site-filling model[32],

$$N(t) = N_{sat}[1 - \exp(-\sigma_{app}\phi t)]$$

where N_{sat} is the saturated concentration, σ_{app} is the apparent trapping cross section, and ϕ is the ion flux density. The curves shown in Figure 12 are the fits to this form. As can be seen from the figure, the initial trapping probability increases with the impact energy, which may be interpreted to result from the increasing efficiency for C-C bond breakage.

Acknowledgement. We are grateful for the financial support from the POSTECH (1987-1989) and the KOSEF (1989-). Useful inputs from professors J. W. Chung, S. K. Paik, and Dr. D. W. Moon for the construction of the instrument are also acknowledged.

References

1. J. A. Barker and D. J. Auerbach, *Surface Sci. Rept.* **4**, 1 (1985).
2. R. B. Bernstein, "Chemical Dynamics *via* Molecular Beam and Laser Techniques", Oxford University Press, Oxford, 1982.
3. T. M. Buck, "Methods of Surface Analysis", edited by A.M. Czanderna, Elsevier, Amsterdam, 1975.
4. J. F. Ziegler, ed., "Ion Implantation Science and Technology", Academic Press, Orlando, 1984.
5. A. H. Agajanian, ed., "Ion Implantation in Microelectronics: A comprehensive Bibliography", Plenum, New York, 1981.
6. S. R. Kasi, H. Kang, C. S. Sass, and J. W. Rabalais, *Surface Sci. Rept.* **10**, 1 (1989).
7. J. Amano and R. P. W. Lawson, *J. Vac. Sci. Technol.* **14**, 831 (1977).
8. H. Kang, S. R. Kai, and J. W. Rabalais, *J. Chem. Phys.* **88**, 5882 (1988).
9. H. Kang, S. R. Kasi, Oscar Grizzi, and J. W. Rabalais, *J. Chem. Phys.* **88**, 5894 (1988).
10. H. Kang, T. S. Schuler, and J. W. Rabalais, *Chem. Phys. Letters* **128**, 348 (1986).
11. S. R. Kasi, M. A. Kilburn, H. Kang, and J. W. Rabalais, *J. Chem. Phys.* **88**, 5902 (1988).
12. H. Akazawa and Y. Murata, *Surface Sci.* **207**, L971 (1989).
13. F. Masson, S. Adura, C. S. Sass and J. W. Rabalais, *Chem. Phys. Letters* **152**, 325 (1988).
14. H. F. Winters and P. Sigmund, *J. Appl. Phys.* **45**, 4760 (1974).
15. D. A. Baldwin, N. Sharmir, P. Hochmann and J. W. Rabalais, *Surface Sci.* **130**, 361 (1983).
16. H. Kang, S. R. Kasi, and J. W. Rabalais, *J. Chem. Phys.* **86**, 3753 (1987).
17. R. Yamada, *J. Vac. Sci. Technol. A* **5**, 2222 (1987).
18. S. R. Kasi, H. Kang, and J. W. Rabalais, *J. Chem. Phys.* **88**, 5914(1988).
19. S. Kasi, H. Kang, and J. W. Rabalais, *Phys. Rev. Letters* **59**, 75 (1987).
20. S. Schubert, U. Imke, W. Heiland, K. J. Snowdon, P. H. F. Reijnen, and A. W. Kleyn, *Surface Sci.* **205**, L793 (1988).
21. M. J. Hayward, Md. A. Mabud, and R. G. Cooks, *J. Am. Chem. Soc.* **110**, 1343 (1988).
22. E. Harting and F. H. Read, "Electrostatic Lenses", Elseivier, Amsterdam, 1976.
23. D. G. Armour, P. Bailey and G. Sharples, *Vacuum* **36**, 769 (1986).
24. St. Halas and B. Adamczyk, *Int. J. Mass Spectrom. Phys.* **10**, 157 (1972).
25. Liliana Deleanu and J. A. D. Stockdale, *J. Chem. Phys.* **63**, 3898 (1975).
26. R. D. Levin and S. G. Lias, eds., "Ionization Potential and Appearance Potential Measurements", U. S. Department of Commerce, 1982.
27. K. C. Smyth, J. A. Schiavone, and R. S. Freund, *J. Chem. Phys.* **59**, 5225 (1973).
28. J. L. Franklin and M. A. Haney, "Recent Development in Mass Spectrometry", edited by K. Ogata and T. Hayakawa, p. 909, University Park, altimore, 1970.
29. A. C. Hurley, *J. Mol. Spectrosc.* **9**, 18 (1982).
30. H. D. Hagstrum, *Surface Sci.* **54**, 197 (1976).
31. D. W. Goodman, R. D. Kelly, T. E. Madey, and J. T. Yates, *J. Catal.* **63**, 226 (1980).
32. D. A. Baldwin, N. Sharmir, and J. W. Rabalais, *Surface Sci.* **141**, 617 (1984).